

# Axial Flow Fan Tip Leakage Flow Control Using Tip Platform Extensions

**Ali Aktürk**

Graduate Research Assistant  
e-mail: aua162@psu.edu

**Cengiz Camci<sup>1</sup>**

Professor  
e-mail: cxc11@psu.edu

Department of Aerospace Engineering,  
Turbomachinery Aero-Heat Transfer Laboratory,  
Pennsylvania State University,  
University Park, PA 16802

*Performance of an axial flow fan unit is closely related to its tip leakage mass flow rate and level of tip/casing interactions. The present experimental study uses a stereoscopic particle image velocimeter to quantify the three dimensional mean flow observed near the blade tip, just downstream of a ducted fan unit. After a comprehensive description of the exit flow from the baseline fan, a number of novel tip treatments based on custom designed pressure side extensions are introduced. Various tip leakage mitigation schemes are introduced by varying the chordwise location and the width of the extension in the circumferential direction. The current study shows a proper selection of the pressure side bump location and width are the two critical parameters influencing the success of each tip leakage mitigation approach. Significant gains in the axial mean velocity component are observed when a proper pressure side tip extension is used. It is also observed that a proper tip leakage mitigation scheme significantly reduces the tangential velocity component near the tip of the axial fan blade. Reduced tip clearance related flow interactions are essential in improving the energy efficiency of ducted fan systems. A reduction or elimination of the momentum deficit in tip vortices is also essential to reduce the adverse performance effects originating from the unsteady and highly turbulent tip leakage flows rotating against a stationary casing. [DOI: 10.1115/1.4001540]*

## 1 Introduction

The flow-field between the stationary casing and the rotor tip of an axial fan is complex because of the interaction of the leakage flow, the annulus wall boundary layer, and the rotor wake. An inherent pressure difference between the pressure and suction sides of the blade tip generates a tip leakage flow that is responsible for a substantial portion of aerodynamic losses in axial flow fans. The leakage flow also rolls into a highly three dimensional tip leakage vortex with significantly turbulent and unsteady flow features in each passage. Tip leakage vortex is a complicated flow phenomenon that is one of the dominant mechanisms of noise generation by unsteady interactions in a turbomachinery system. It is also one of the major energy loss mechanisms for the axial flow fan systems. Despite the close relation between the tip leakage flow and the performance of axial fans, there has been limited amount of information about the three dimensional flow structure of leakage vortex in open literature [1–4].

Inoue et al. [5] made detailed flow measurements before and behind an axial flow rotor with different tip clearances. In their study, they investigated the clearance effect on the behavior of the tip leakage flow. Furukawa et al. [6] also investigated the breakdown of the tip leakage vortex in a low speed axial flow compressor. Reducing the tip leakage mass flow rate improves the aerodynamic performance of axial flow fans and compressors. Implementation of treatments in the nonrotating part over the blade tip is also an efficient way of tip leakage flow reduction. References [7,8] investigate different casing treatments for axial flow compressors.

The wake developed from an axial flow fan has a strong influence on the system performance. It is a significant source of aerodynamic loss and affects the efficiency and vibration characteristics. References [9–11] deal with extensive investigations of the

wake flow features such as mean velocities, turbulence, and decay characteristics on the turbomachinery performance.

Stereoscopic particle image velocimetry (SPIV) is an effective way of measuring all three velocity components of an instantaneous flow-field over a selected area [12–16]. A comprehensive discussion of the specific SPIV technique used in this paper is given by Kahveci and Camci [13–15]. Yoon and Lee [16] investigated the flow structure around an axial flow fan using the SPIV technique. The time averaged results clearly show the evolution and dissipation of tip vortices. Yen and Lin [17] analyzed the exit flow performance and properties of an axial flow fan with winglet-blades at various impeller angles using SPIV. The velocity profiles show the most stable and the best fan performance resulting from winglet-blades, which increase the lift and reduce the drag. Wernet et al. [18] made phase-locked three-dimensional digital particle image velocimetry (DPIV) measurements near the tip region of a low speed compressor rotor to characterize the behavior of the rotor tip clearance flow. A comparison of the DPIV measurements to the Navier–Stokes flow simulations was also done.

Corsini et al. [19–22] presented the results of a computational study of an axial flow fan using “improved tip concepts.” The first two end-plates were with constant and variable thickness distributions, while the last two were designed by combining the end-plates with a stepped gap on the tip. The investigation was based on a finite element Navier–Stokes solver for the physical interpretation of the detailed 3D leakage flow-field. The specific fan performance experiments have shown that the improved tip concepts introduced a small performance derating, but the efficiency curves give evidence of an improvement with a better peak performance and a wider high efficiency curve toward the rotor stall margin. An aero-acoustic investigation showed a reduction in the rotor aero-acoustic signature.

The computationally predicted loss coefficients in Ref. [22] showed that the highest loss regions were always observed near the leakage vortex core. The computational comparison of mechanical energy loss within the gap showed that the tip end-plates lead to a reduction in mechanical energy loss within the gap.

The present experimental study used stereoscopic particle image velocimetry measurements at the exit of the seven-bladed

<sup>1</sup>Corresponding author.

Contributed by the Fluids Engineering Division of ASME for publication in the JOURNAL OF FLUIDS ENGINEERING. Manuscript received July 17, 2009; final manuscript received February 20, 2010; published online May 14, 2010. Assoc. Editor: Zvi Rusak.

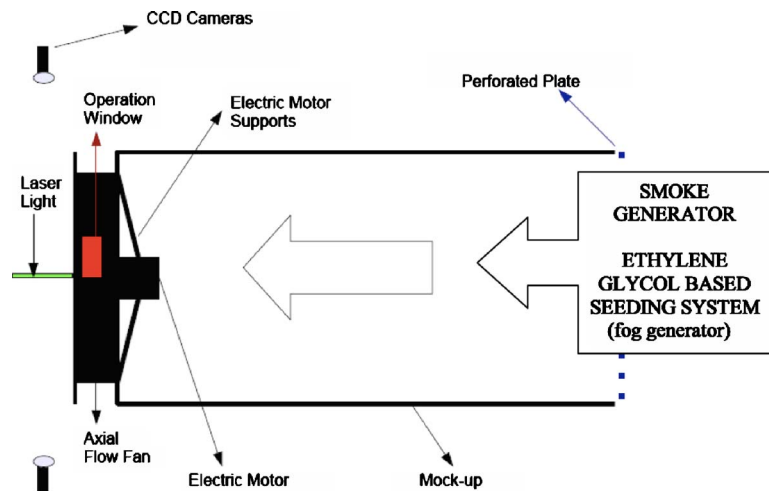


Fig. 1 Test rig and stereoscopic SPIV setup

axial fan rotor. The fan rotor used for the experiment is widely used in the air conditioning industry. All of the experiments were performed at constant rotational speed of the fan (859 rpm).

The main objectives of the current study are summarized as follows:

- to investigate the characteristics of tip leakage flow and tip vortex in an axial flow fan using a high spatial resolution and nonintrusive measurement technique; all three components of the tip region exit flow-field are measured using the SPIV technique
- to eliminate the adverse effects of the tip vortex by designing novel rotor tip geometries using pressure side extensions
- to reduce the local leakage mass flow rate and momentum deficit in tip-vortex-driven flow structures
- to increase the energy efficiency of axial flow fan systems
- to provide high quality phase-locked instantaneous flow data for further studies in aero-acoustics of tip treated axial flow fans

## 2 Experimental Setup

**2.1 Test Rig.** The test rig that consists of an axial flow fan, a mock-up unit, and an electric drive system, as shown in Fig. 1, was designed to investigate the rotor exit flow phenomena using a SPIV system. The setup also has provisions for seeding the fan flow-field with a smoke generator using a fluidized bed. The smoke generator is located near the inlet section of the mock-up unit where a perforated plate controlling the fan loading is mounted. The electric motor driving the fan rotor is speed controlled by an AC inverter unit. The current phase-locked SPIV measurements are triggered by using an optical once-per-revolution device located near the hub of the rotor inlet. An infrared beam is reflected from a highly reflective surface attached to the rotor hub. This once-per-revolution pulse provides a phase-locked triggering of the SPIV data collection system. The relative position of the rotor can be adjusted accurately in relative to the position of the laser light sheet that contains the rectangular SPIV measurement area.

**2.2 Ducted Fan.** Figure 2 shows a seven-bladed axial flow fan unit including the orientation of the SPIV system components. The geometric specifications are presented in Fig. 3. A perforated plate at the inlet section of the mock-up unit is used for creating realistic fan loading conditions. The tips of the blades are modified through a removable “operation window,” as shown in Fig. 1. Only one blade tip out of seven blades is modified since the current SPIV system is capable of measuring in the immediate vicinity of a “selected” blade tip due to the phase-locked and instant-

aneous nature of the SPIV measurements. A precision machined 0.762 mm (0.030 in.) thick thermoplastic layer was used for the selected tip platform design. The tip platform design was attached to the precision machined tip area in a nonintrusive way through the operation window, as shown in Fig. 1. The modifications made on the selected tip did not cause a measurable rotor balance problem since the rotor was manufactured out of a relatively light weight thermoplastic material. The current rotor blades have serrated trailing edges for effective mixing of the blade boundary layers in the wake of each blade. The serrated trailing edges also provide an effective mixing of individual tip vortices with the wakes of the seven blades in the rotating frame of reference. It should be noted that the comparison of the flow with serrated trailing edges with a smooth trailing edge flow is not the subject of the current paper.

**2.3 Fan Performance.** The performance of the fan unit is measured under three different loading conditions. The first performance point ( $80 \text{ m}^3, 140 \text{ Pa}$ ) shown in Fig. 4 is obtained by using a perforated steel plate having an open area ratio of 19.6%. A second perforated plate using a slightly larger open area ratio of 42.5% provides the middle point ( $280 \text{ m}^3/\text{min}$ ,  $88 \text{ Pa}$ ) in the performance curve, as shown in Fig. 4. The third point with the highest volumetric flow rate at  $340 \text{ m}^3/\text{min}$  is obtained when there is no perforated plate installed at the inlet section of the mock-up unit. The pressure change across the fan is measured by using pitot static holes mounted on all four sides of the mock-up unit. Wall-static pressures from all four sides are averaged. For the mass flow rate measurements, a hot-wire-based volumetric flow measurement device is used at the rotor downstream.

**2.4 SPIV System.** The PIV technique measures instantaneous velocity components of a flow-field over a determined area. Small particles that go with the flow are introduced into the fluid flow, and the region of interest is illuminated by the light sheet provided by subsequent Nd:YAG (yttrium aluminum garnet) laser pulses lasting as short as a few nanoseconds. The subsequent step is the recording of the displacement of particles via two high sensitivity CCD cameras.

The scattered light from the seeding particles is recorded by two different cameras for simultaneous recording on digital media. The initial position of a particle is recorded on the first frame of the camera right after the first laser pulse fires. In general, a typical duration of a laser pulse is about 30 ns in a flow-field similar to the current study. Its final position is recorded in the same way on the second frame of the same camera when the second laser pulse fires. The time interval between the two frames is usually determined by the mean flow speed in the area of in-

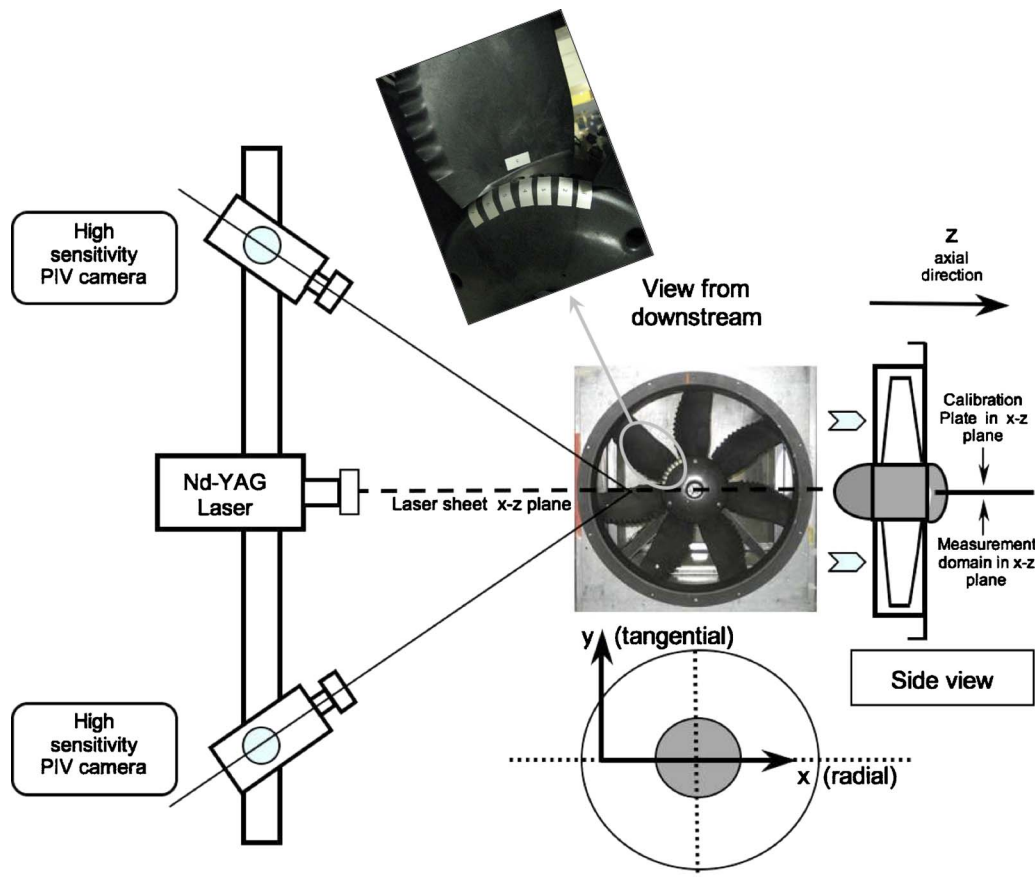


Fig. 2 Axial flow fan as seen from the exit plane and the SPIV system orientation

vestigation. The order of magnitude of this adjustable time separation between the two frames is “microseconds.” Since the displacement of the particle and the time interval between the two subsequent laser pulses are known, the velocity of the particle can be calculated by the simple equation speed=distance/time. A comprehensive explanation of this technique is given in Refs. [12–16].

In 3D PIV, there is an additional camera viewing the field from a different angle. The two-dimensional image obtained by each camera is slightly different from each other, and afterwards, they are combined to produce the three-dimensional velocity information. Stereoscopic vision principles are instrumental in this process of combining the two planar images obtained from the two cameras viewing the same flow-field simultaneously. The data reduction in a SPIV system requires the processing of four independent images from the two cameras. For 3D analysis, the 2D calibration images need to be converted additionally into the 3D data by a direct linear transform (DLT) model in order to calculate the third component of the velocity. Correlation techniques are used to obtain raw vector maps out of image pairs taken during the experiments, and a number of calculation methods are used to evaluate these vector maps. In summary, the three dimensional space defined by the planar measurement area and the finite thickness of the laser sheet is analytically described in relation to the highly distorted images captured by the two CCD chips in each of the two cameras. The distortions observed on the planar CCD images are generated by the angled position of the two cameras. For example, a perfect cube in the measurement space is seen as a distorted cube in each one of the two images generated by the two cameras.

The current study uses high sensitivity cameras that are essential in high speed flow measurements. Two of the 80C60 HiSense PIV/PLIF cameras with  $1024 \times 1280$  pixels are used with 80N57

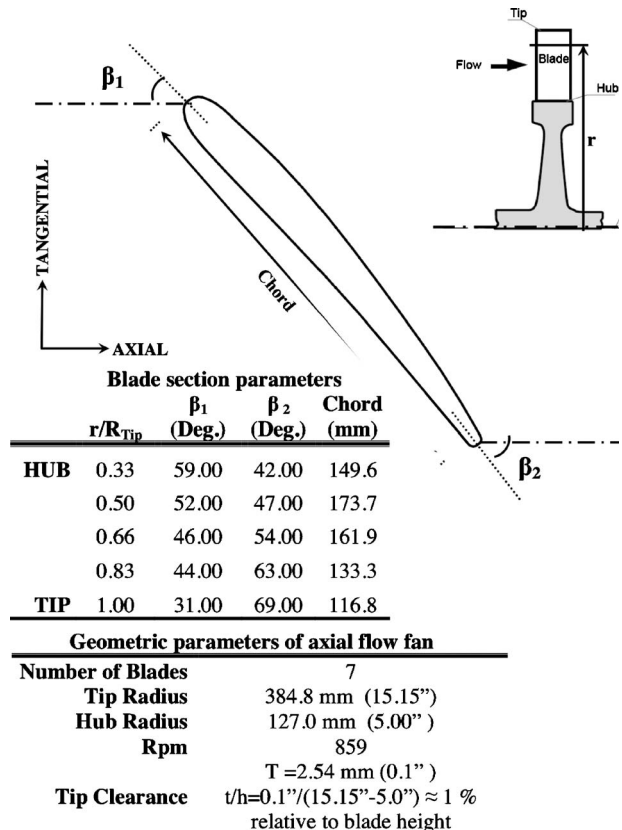


Fig. 3 Geometric and blade section parameters of the axial flow fan

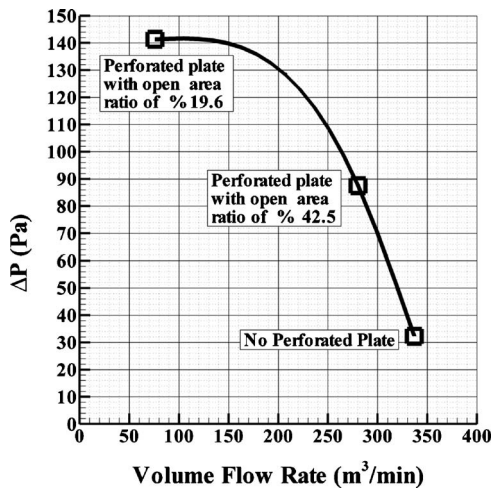


Fig. 4 Axial flow fan performance

personality module fitted to processor and a Nikon micro-Nikkor 60/2.8 objective for each camera. The calibration plate, the cameras, the Nd:YAG pulsed laser unit, and the axial fan rotor blades are shown in Fig. 2. The initial calibration procedure requires that the laser light sheet generated by the Nd:YAG laser is aligned with the calibration plate carrying a standard high precision square grid.

### 3 Experimental Methodology

**3.1 Measurement Domain.** The axial ( $y$ ), radial ( $x$ ), and tangential ( $z$ ) components of velocity profiles were simultaneously measured near the tip region of the fan under the influence of a few novel tip platform extensions designed throughout this investigation. Figure 5 shows the measurement domain, which is a rectangle in the  $x$ - $y$  plane located just downstream of the rotor. The  $x$ - $y$  plane is horizontal and contains the axis of rotation. Most of the SPIV distributions covered a spanwise region from  $r/R_{tip} = 0.6$  to  $r/R_{tip} = 1.3$ . This measurement area corresponds to a region covering the last three quarters of the blade height, including the tip region flow. The spanwise velocity distributions shown in Figs. 8–11 are obtained at an axial position 46 mm away from the rotor exit plane. The radial direction is also marked with  $r/R_{tip}$  in order to mark the exact position of the blade root and tip in the spanwise distributions of velocity.  $r/R_{tip}$  is approximately 0.33 at the blade root location (hub).

**3.2 Specific Rotor Positions for Phase-Locked Measurements.** The results from the custom designed tip platform extensions are compared with the results obtained from a

Table 1 Uncertainties of ensemble averaged velocity components

	Radial velocity	Axial velocity	Tangential velocity
$N=50$	$1.19 \times 10^{-1} U_a$	$1.11 \times 10^{-1} U_a$	$1.98 \times 10^{-1} U_a$
$N=100$	$7.47 \times 10^{-2} U_a$	$6.44 \times 10^{-2} U_a$	$1.28 \times 10^{-1} U_a$
$N=150$	$6.01 \times 10^{-2} U_a$	$4.85 \times 10^{-2} U_a$	$8.89 \times 10^{-2} U_a$
$N=200$	$4.77 \times 10^{-2} U_a$	$3.97 \times 10^{-2} U_a$	$7.93 \times 10^{-2} U_a$
$N=250$	$3.99 \times 10^{-2} U_a$	$3.39 \times 10^{-2} U_a$	$6.68 \times 10^{-2} U_a$

baseline tip at two different tip clearance levels. All three components of the velocity vector were measured for seven circumferential positions of the rotor (with respect to the SPIV measurement plane). These locations were chosen by dividing the rotor blade pitch into seven equiangular regions. Although the measurements were performed at seven positions, only the most pertinent data from three selected positions are presented. The selected positions include blade tip leading edge, midchord, and trailing edge (locations 3, 4, and 5).

**3.3 Statistical Stability of SPIV measurements.** An adequate number ( $N$ ) of SPIV speckle images should be recorded and processed for satisfying the statistical requirements for accurate mean velocity measurements. The ensemble average of measured velocity components approaches a true mean as  $N$  goes to infinity. During an ensemble averaging of finite number of instantaneous velocity measurements, it should be noted that their average may have a deviation from the true mean value. This deviation is closely related to the sample size ( $N$ ), which is a measure of the statistical stability of this ensemble averaging process. Table 1 shows deviations calculated from the measured data for the radial, axial, and tangential velocity components obtained by averaging 50, 100, 150, and 250 PIV speckle images. Standard errors are calculated by using the central limit theorem [23]. The central limit theorem states that uncertainty can be approximately equal to the standard deviation of measured values ( $\sigma$ ) divided by  $\sqrt{N}$  (i.e.,  $\epsilon = \sigma / \sqrt{N}$ ). The uncertainties are estimated at locations of the highest standard deviations of individual components for each sampling image size. They are normalized by using averaged axial velocity ( $U_a$ ) calculated from the mass flow rate of the fan for the condition that experiments are conducted (340 m³/min, 32 Pa). Note that the most uncertainties are smaller than 9% for the ensemble image size of more than 150 images.

Based on the examination of data convergence with the number of speckle images, the sampling image size ( $N$ ) is selected to be 170. Figure 6 presents the influence of the ensemble averaging sample size on the spanwise distribution of the most significant velocity component “axial component.” The baseline blade tip is used in this experiment with a nominal tip clearance of 1% of the

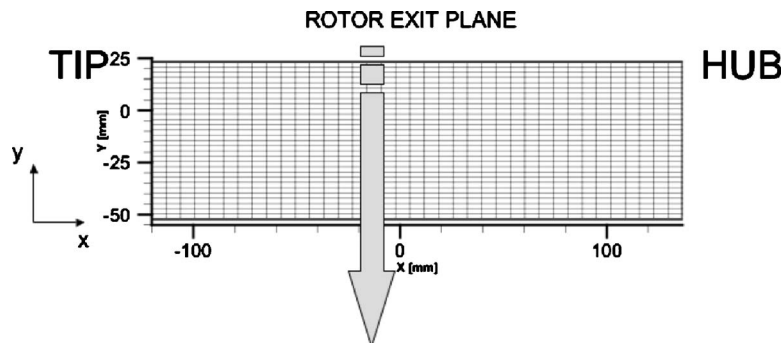


Fig. 5 SPIV measurement plane (horizontal) downstream of the rotor exit and the coordinate system



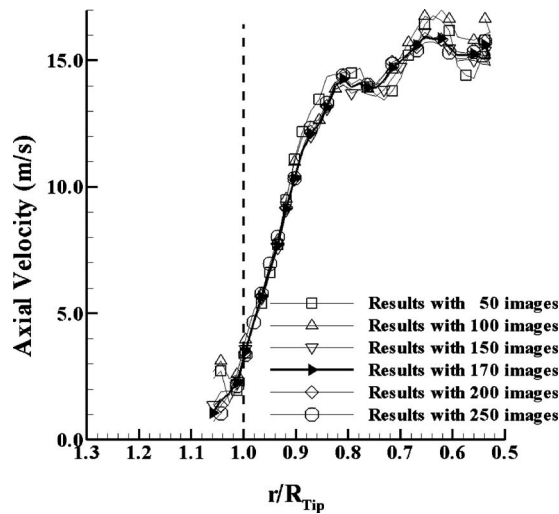


Fig. 6 Influence of the sample size on SPIV ensemble averaging

blade height. The spanwise region where  $0.9 \leq r/R_{tip} \leq 1.02$  is not significantly influenced from the choice of the ensemble averaging sample size. The sample sizes of 150, 170, 200, and 250 produce very similar spanwise distributions in this region near the tip. All SPIV experiments presented in Figs. 8–13 are conducted using an ensemble averaging sample size of 170.

**3.4 Tip Clearance Values.** An effective control of the tip leakage flow was achieved using different tip platform extensions. The term “control of tip leakage flow” in this study could be defined as the “minimization of tip leakage flow mass flow rate.” The baseline profile was evaluated at two different tip clearance values of 0.1 in. and 0.135 in., corresponding to 1% and 1.35% of the blade height. All of the “tip platform extensions” used in this study were evaluated at tip clearance values of 0.1 in., corresponding to 1% of the blade height.

**3.5 The General Impact of Tip Platform Extensions.** The main goal of this study is to minimize the tip leakage flow by interfering with the flow near the pressure side corner of the blade tip region. A new static pressure distribution near the blade tip section is established by the novel tip platform extension designs shown in Fig. 7.

The impact of the suggested tip platform extensions is visible in the “magnitude enhancements” of the axial velocity component downstream of the tip region. It is also highly visible that the strong tangential velocity components induced by the baseline tip

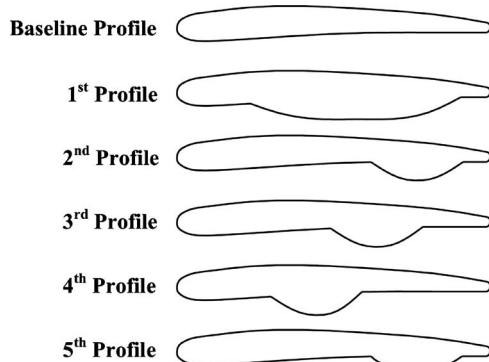


Fig. 7 Novel tip platform extensions for tip leakage mitigation

are almost eliminated by an effective tip platform design. This observation is very clear, especially near the tip diameter of the rotor exit flow.

**3.6 Geometrical Definition of the Five Tip Platform Extensions.** The design idea behind the present tip platform extensions is based on estimating the blade chordwise position where the tip leakage potential is the highest for a given tip profile. It is obvious that the leakage potential is represented by the static pressure differential imposed by the shape design of the blade profile. The initial computational fluid dynamics based flow prediction may be effective in finding the chordwise region where the leakage mass flow rate is maximum.

The tip platform extensions were designed by adding constant-thickness “pressure side bumps” of different designs to the base profile, as shown in Fig. 7. The thickness of the platform extended on the pressure side of the blade is about 0.030 in. (0.762 mm) for all designs used in this investigation. Initially, a wide bump between the trailing edge and the leading edge was suggested as Profile 1 in Fig. 7. The maximum width of the bump was chosen as the same as the thickness of the airfoil at the bump centerline location. Three more tip platform extensions were derived from Profile 1 by dividing the bump width of Profile 1 into three almost equal chordwise sections. The three new tip platform extensions are termed Profile 2 (near the trailing edge), Profile 3 (middle of the wide bump), and Profile 4 (almost midchord). The bump maximum widths were kept the same. Profile 5 is a derivative of the trailing edge bump named as Profile 2. Profile 5 uses a relatively small platform area when compared with all other tip platform extensions. The external contour of Profile 5 is almost parallel to the baseline profile, except the end points where blending is suggested.

Only one rotor blade at a time out of seven blades was retrofitted with a suggested design. Each experiment had six baseline blades and a seventh blade with the suggested tip platform extension. The effective clearance was kept same for all seven blades.

## 4 Experimental Results and Discussion

Figures 8–11 show the results of the exit flow measurements of the axial flow fan at the highest volumetric flow rate condition defined as 340 m<sup>3</sup>/min, 32 Pa. Figure 12 complements these results from a data set obtained at the minimum mass flow rate condition where the pressure loading is maximum (80 m<sup>3</sup>/min, 140 Pa). All the velocity profiles are plotted at 1.811 in. (46 mm) downstream of the fan.

In addition to the magnitude of the velocity vector (total velocity), the radial, tangential, and axial components of the velocity vector at the exit of the rotor are provided in function of the spanwise distance.

**4.1 Baseline Tips.** Near the tip, where  $r/R_{tip} \geq 0.9$ , the two base profiles show very similar trends in Fig. 8. The total velocity is significantly reduced in the core of the passage, where  $r/R_{tip} \leq 0.9$ , when the tip clearance is high at 0.135 in. level. The  $t = 0.100$  in. and  $t = 0.135$  in. clearance base profiles show significant momentum deficit occurring in the core of the tip vortices from the two baseline tips (without any tip platforms). The tip vortices from the baseline cases greatly influence the core flow and reduce the mean kinetic energy when they are mixed with the wake fluid. The wake fluid and the tip leakage vortex are also modified and mixed by the serrated trailing edge geometry, as shown in Fig. 2. This observation indicates that a significant momentum deficit in the core of the passage vortex exists because of the tip vortex, and this momentum deficit becomes higher when the clearance increases. The direct impact of the baseline tip vortex is visible in the measured total velocity in the core of the passage, even under strong mixing conditions induced by the wake fluid originating from the serrated trailing edges.

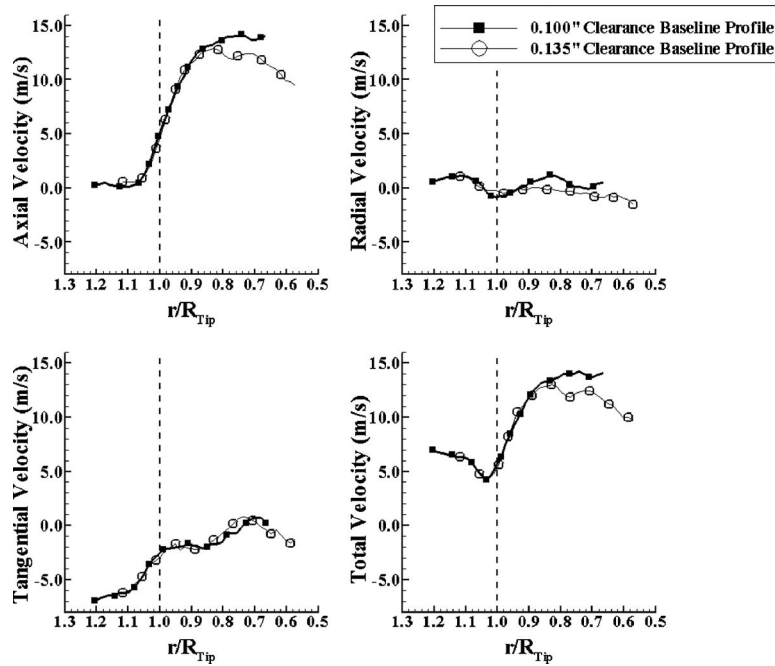


Fig. 8 Velocity profiles measured at location 3 for two different tip clearances

**4.2 The Radial Component.** The radial components for all cases, as shown in Figs. 8–12, are all very small magnitudes, around  $\pm 1$  m/s. There is no significant influence on the magnitude of the baseline clearance or the type of tip treatment on the magnitude of the radial component at all spanwise locations.

**4.3 Influence of Tip Platform Extensions on the Tangential Component.** When the axial velocity component in Fig. 9 is compared with the total velocity, a striking observation in the tip region is apparent. The total velocity for the baseline tips is much higher than the axial component, where  $r/R_{tip} \geq 1.05$ . However,

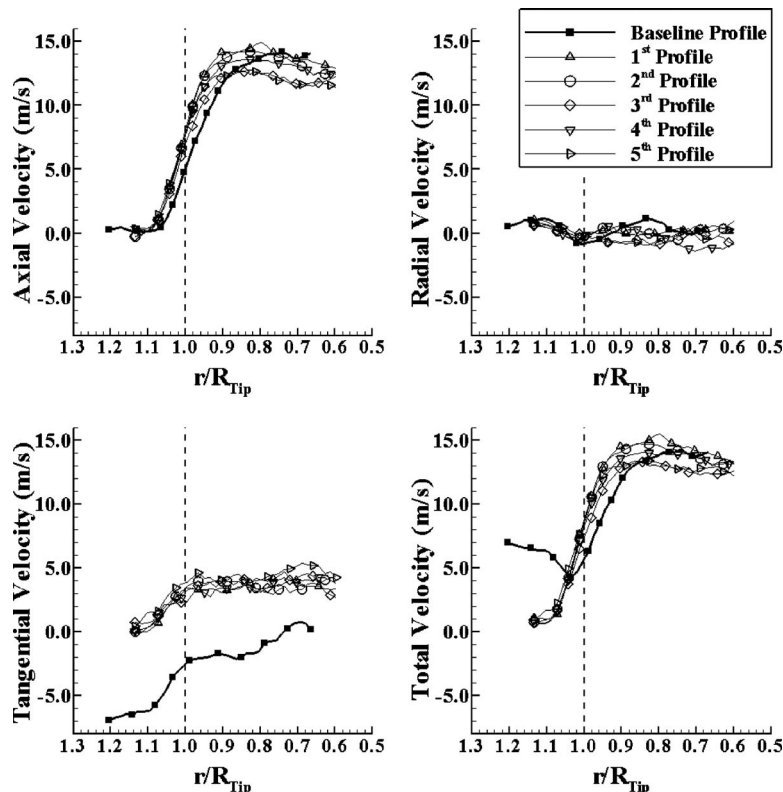


Fig. 9 Velocity profiles measured at location 3 (340 m<sup>3</sup>/min, 32 Pa)

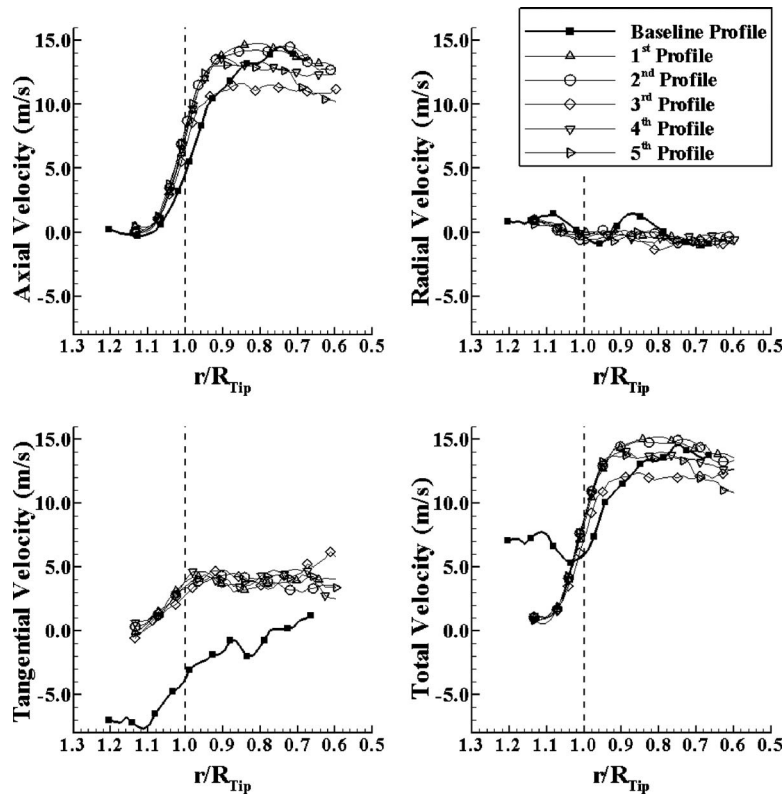


Fig. 10 Velocity profiles measured at location 4 (340 m<sup>3</sup>/min, 32 Pa)

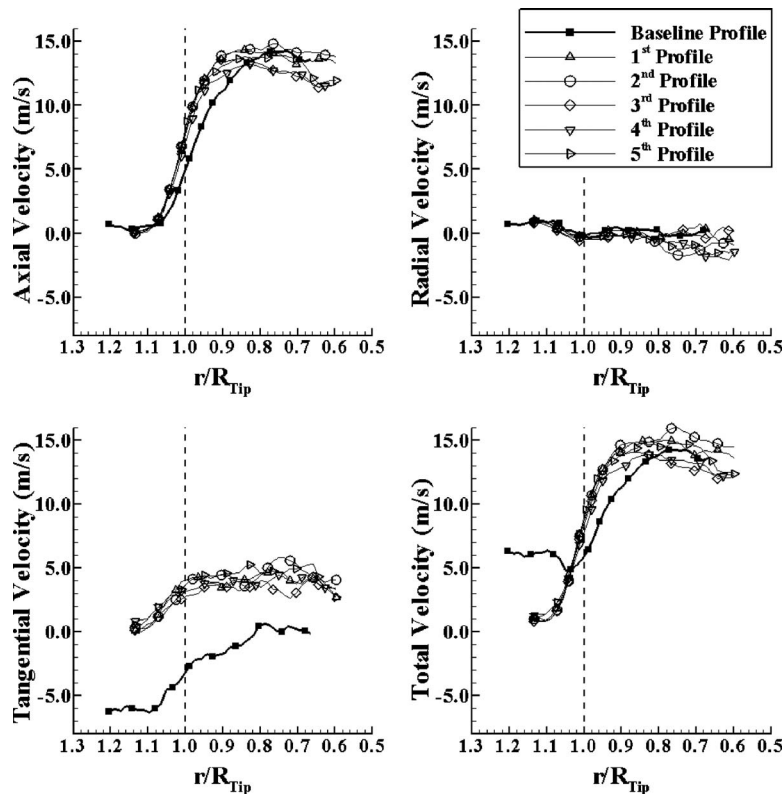


Fig. 11 Velocity profiles measured at location 5 (340 m<sup>3</sup>/min, 32 Pa)

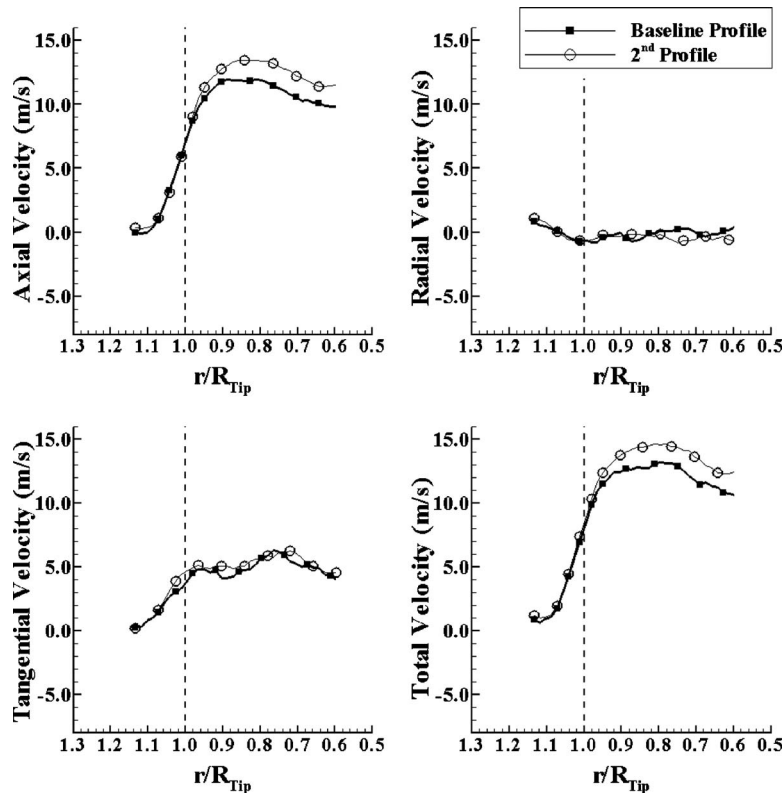


Fig. 12 Velocity profiles measured at location 3 (high  $\Delta P$  with 19.6% perforated plate, 80 m<sup>3</sup>/min, 140 Pa)

the total velocity distribution for baseline tips is about the same as the axial velocity component for the five treated tips shown in Fig. 8. Since the radial components are extremely small for all tip shapes, one can infer that the significant difference between the baseline and treated tips is due to a strong change in the tangential component of the velocity vector. The distribution of the tangential component shows a significant difference in the whole measurement region, where  $r/R_{tip} \geq 0.6$ .

One can conclude that there is a strong swirl component near the tip region when there is no tip treatment. The five treated tips defined in Fig. 7 provide significant reduction in the amount of swirl in the rotor exit flow. The reduction in the amount of swirl near the tip region is about 4–5 m/s, with the tip platform extensions shown in Fig. 7. The magnitude of the swirl component that is inherent to baseline tips is about one-third of the total velocity existing in the core of passage.

**4.4 Tip Platform Extensions With Highest Axial Velocity at Rotor Exit.** Figure 9 shows that the five new tip platform extension devices can be highly instrumental in reducing the amount of swirl coming out of the rotor. This feature is certainly a benefit in terms of the energy efficiency of the axial flow fan when the fan is operated on its high volumetric flow rate (low pressure rise) point. The tip platform extensions help to reduce the tip leakage mass flow rate and its momentum deficit via local viscous flow modifications near the tip region. Profiles 1 and 2 provide the two profiles with the highest total velocity in the core of the passage exit flow.

**4.5 The Optimal Tip Platform Design.** The experimental results suggest that the “maximum width” of the bump is an important parameter in designing the tip desensitization geometry. Profiles 2 and 5 cover almost the same chordwise locations. The only difference between the two is the maximum width of the bump. Figures 8–10 clearly show that the recovery of the axial velocity component and elimination of the tangential component

is more effective with Profile 2 than with Profile 5. Figures 9–11 show that the features observed in Fig. 9 for location 3 repeat for other angular positions of the rotor (locations 4 and 5). Although there are slight flow-field differences at different rotor positions, the general nature of the discussion does not change.

**4.6 Fan Exit Flow at the Highest Pressure Rise.** An interesting tip treatment experiment could be performed by operating the fan at its highest pressure point by reducing the volumetric flow rate using a perforated steel plate at the mock-up inlet section, as shown in Fig. 1. The experiments with the specific perforated plate with an open area ratio of 19.6% indicated that measurable gains in axial velocity component at the core of the exit flow still exist with Profile 2. Figure 12 shows that the tangential and radial velocity components from Profile 2 are very similar to the baseline profile at the same effective clearance value of 0.100 in. (1%). However, the elimination of the tangential component observed in high volumetric flow rate experiments does not occur under high pressure rise conditions (140 Pa), as shown in Fig. 12. There is a consistent 2 m/s increase in axial (or total) velocity throughout the blade span when  $r/R_{tip} \geq 0.6$ . Under high loading conditions, the swirl component is minimal even with a baseline tip. The tip platform extensions for this case also perform their function by minimizing the tip leakage flow mass flow rate. The minimization of the tip leakage mass flow rate eventually provides the gain in axial (or total) velocity component. On the average, the gain in the total velocity magnitude at the rotor exit is about 17% throughout the blade span. This type of gain in the mean kinetic energy of the fan exit flow is expected to contribute to the energy efficiency of the fan.

**4.7 Rotor Exit Total Velocity Distributions.** Figures 13 and 14 show total velocity contours drawn on the axial and radial planes at the fan rotor exit for baseline tip and Profile 2, respectively. Both contours are obtained from measurements performed at a 0.1 in. tip clearance. The rotor tip ( $r/R_{tip} = 1.0$ ) is marked with



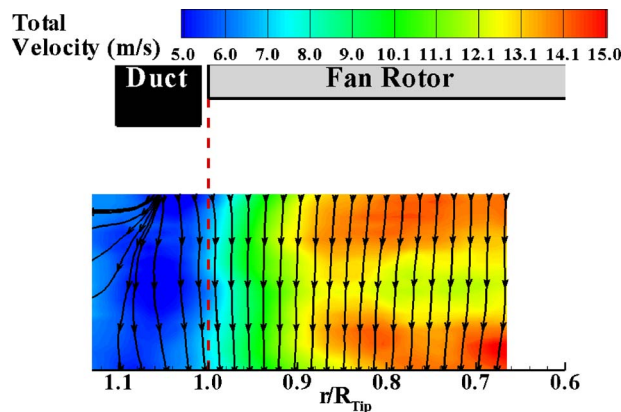


Fig. 13 Total velocity contour and streamlines at location 3 for baseline profile (340 m<sup>3</sup>/min, 32 Pa)

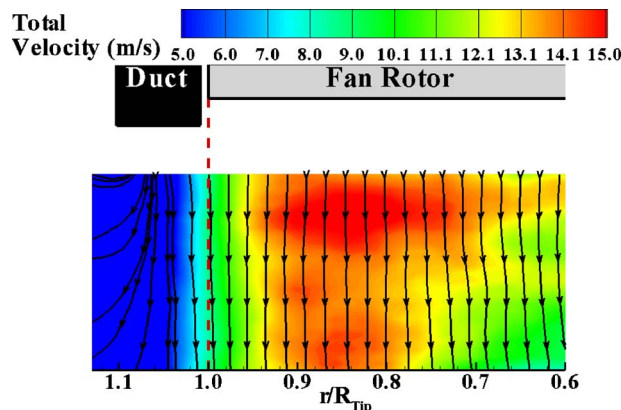


Fig. 14 Total velocity contour and streamlines at location 3 for the 2nd profile (340 m<sup>3</sup>/min, 32 Pa)

the dashed line. An enhancement of total velocity near the tip region is observed when the tip region total velocities are compared. It is also obvious that using Profile 2 enhances the area coverage of a high momentum jet at the exit. That means the rotor blade with a tip platform Profile 2 increases the kinetic energy of the fluid flow more efficiently. It also reduces the momentum deficit near the tip due to the tip leakage flow.

**4.8 Influence of Tip Platform Extensions on the Flow Coefficient.** The positive effect of the five new tip platform extensions on flow coefficient of the fan rotor is shown in Fig. 15. Flow coefficient is plotted at 46 mm downstream of the fan. For  $r/R_{tip} \geq 0.9$  (near the tip region), all the tip platform extensions increased the flow coefficient. This increase is related to the increase in axial velocity near the tip region due to tip treatments. Measurable reduction in the tangential velocity component resulted in a measurable increase in the flow coefficient. Profiles 1 and 2 are the two profiles with the highest flow coefficient in the core of the passage exit flow. Profiles 3, 4, and 5 slightly increase the flow coefficient near the tip region, but they provide with lower flow coefficient in the core flow region. The lower flow coefficient in the core may be attributed to the specific location of the platform extensions. On the average, the gain in the flow coefficient from Profiles 1 and 2 at the rotor exit is about 18.6% throughout the blade span.

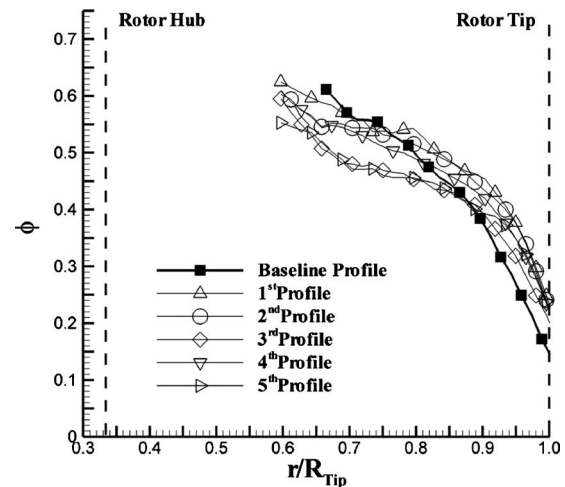


Fig. 15 Flow coefficient calculated at location 3 (340 m<sup>3</sup>/min, 32 Pa)

## 5 Conclusions

Novel tip platform extensions for energy efficiency gains and aero-acoustic improvements were designed for an axial flow fan where wake mixing is already enhanced with a serrated trailing edge design.

Five different tip platform extensions were introduced especially on the pressure side of the fan blades.

It is possible to reduce the tip leakage mass flow rate using the novel tip platform extensions. Profile 2 showed the best tip treatment performance out of the five new tip platform extensions designed in this investigation.

Tip treatment experiments performed at a high volumetric flow rate/low pressure rise clearly showed the minimization of the tip vortex mass flow rate by significantly reducing the tangential components near the tip.

The tip platform extensions on the pressure side have proven to be effective swirl reducing devices at the exit of the fan. The magnitude of this reduction is about one-third of the rotor exit total velocity in the core of the passage exit.

The reduction in the tip leakage mass flow rate produced enhanced total velocity values between the midspan and the tip at the passage exit.

Tip platform experiments performed at the highest pressure point by reducing the volumetric flow rate using a perforated steel plate at the mock-up inlet section also showed a significant tip leakage control for the fan. However, the elimination of the tangential component observed in high volumetric flow rate experiments does not occur under high pressure rise conditions.

Under high loading conditions, the swirl component is minimal even with a baseline tip. With the tip platform extension "Profile 2," there is a consistent 2 m/s increase in axial (or total) velocity throughout the blade span when  $r/R_{tip} \geq 0.6$ .

Tip platform extensions perform their function by minimizing the tip leakage flow mass flow rate near the blade tip even under the high loading conditions. This effect eventually provides the gain in axial component.

On the average, the gain in the total velocity magnitude at the rotor exit is about 17% throughout the blade span. This type of gain in the mean kinetic energy of the fan exit flow is expected to contribute to the energy efficiency of the fan.

## Acknowledgment

The authors acknowledge the major support from the Vertical Lift Rotorcraft Center of Excellence (VLRCE) of the Department of Aerospace Engineering at Penn State University. This research is partially funded by the U.S. government under Agree-

ment No. W911W6-06-2-0008. The authors also acknowledge the technical support of Mr. H. Houtz during the experiments.

## Nomenclature

- $\beta_1$  = blade section inlet angle  
 $\beta_2$  = blade section exit angle  
 $c$  = chord length  
 CCD = charge-coupled device  
 $\epsilon$  = experimental uncertainty  
 $h$  = blade height  
 $N$  = number of SPIV speckle images  
 PLIF = phosphorescence laser-induced fluorescence  
 $p$  = static pressure  
 $\phi$  = flow coefficient,  $\phi = U/\omega r$   
 $r$  = radial position ( $r=0.0$  at the axis of rotation)  
 $R_{\text{hub}}$  = hub radius  
 $R_{\text{tip}}$  = tip radius  
 $\sigma$  = standard deviation  
 $t$  = effective tip clearance in inches  
 $U$  = axial velocity  
 $V$  = radial velocity  
 $W$  = tangential velocity  
 $U_a$  = averaged axial velocity  
 $\omega$  = rotational speed  
 $x$  = radial direction, see Fig. 2  
 $y$  = axial direction, see Fig. 2  
 $z$  = tangential direction, see Fig. 2

## References

- [1] Lee, G. H., Baek, J. H., and Myung, H. J., 2003, "Structure of Tip Leakage in a Forward-Swept Axial-Flow Fan," *Flow, Turbul. Combust.*, **70**, pp. 241–265.
- [2] Jang, C. M., Furukawa, M., and Inoue, M., 2001, "Analysis of Vertical Flow Field in a Propeller Fan by LDV Measurements and LES—Parts I, II," *ASME J. Fluids Eng.*, **123**, pp. 748–761.
- [3] Storer, J. A., and Cumpsty, N. A., 1991, "Tip Leakage Flow in Axial Compressors," *ASME J. Turbomach.*, **113**, pp. 252–259.
- [4] Lakshminarayana, B., Zaccaria, M., and Marathe, B., 1995, "The Structure of Tip Clearance Flow in Axial Flow Compressors," *ASME J. Turbomach.*, **117**, pp. 336–347.
- [5] Inoue, M., Kuroumaru, M., and Furukawa, M., 1986, "Behavior of Tip Leakage Flow Behind an Axial Compressor Rotor," *ASME J. Eng. Gas Turbines Power*, **108**, pp. 7–14.
- [6] Furukawa, M., Inoue, M., Kuroumaru, M., Saik, K., and Yamada, K., 1999, "The Role of Tip Leakage Vortex Breakdown in Compressor Rotor Aerodynamics," *ASME J. Turbomach.*, **121**, pp. 469–480.
- [7] Fujita, H., and Takata, H., 1984, "A Study on Configurations of Casing Treatment for Axial Flow Compressors," *Bull. JSME*, **27**, pp. 1675–1681.
- [8] Moore, R. D., Kovich, G., and Blade, R. J., 1971, "Effect of Casing Treatment on Overall and Blade-Element Performance of a Compressor Rotor," NASA Report No. TN-D6538.
- [9] Reynolds, B., Lakshminarayana, B., and Ravindranath, A., 1979, "Characteristics of Near Wake of a Fan Rotor Blade," *AIAA J.*, **17**, pp. 959–967.
- [10] Ravindranath, A., and Lakshminarayana, B., 1980, "Mean Velocity and Decay Characteristics of Near and Far-Wake of a Compressor Rotor Blade of Moderate Loading," *ASME J. Eng. Power*, **102**, pp. 535–547.
- [11] Myung, H. J., and Baek, J. H., 1999, "Mean Velocity Characteristics Behind a Forward-Swept Axial-Flow Fan," *JSME Int. J., Ser. B*, **42**, pp. 476–488.
- [12] Adrian, R., 1991, "Particle Imaging Techniques for Experimental Fluid Mechanics," *Annu. Rev. Fluid Mech.*, **23**, pp. 261–304.
- [13] Kahveci, H. S., and Camci, C., 2006, "Flow Around Helicopter Blade Tip Sections Using 2D Particle Image Velocimeter—Part I," 11th International Symposium on Transport Phenomena and Dynamics of Rotating Machinery (ISROMAC-11), (136).
- [14] Kahveci, H. S., and Camci, C., 2006, "Flow Around Helicopter Blade Tip Sections Using a (3D) Stereoscopic Particle Image Velocimeter—Part II," 11th International Symposium on Transport Phenomena and Dynamics of Rotating Machinery (ISROMAC-11), (137).
- [15] Kahveci, H. S., 2004, "Implementation of a SPIV in Rotating Machinery Including Helicopter Rotor Flows," MS thesis, Pennsylvania State University, University Park, PA.
- [16] Yoon, J. H., and Lee, S. J., 2004, "Exit Flow Field and Performance of Axial Flow Fans," *Exp. Therm. Fluid Sci.*, **28**, pp. 791–802.
- [17] Yen, S. C., and Lin, F. K. T., 2006, "Exit Flow Field and Performance of Axial Flow Fans," *ASME J. Fluids Eng.*, **128**, pp. 332–340.
- [18] Wernet, M. P., Van Zante, D., Strazisar, T. J., John, W. T., and Prahst, P. S., 2005, "Characterization of Tip Clearance Flow in an Axial Compressor Using 3D DPIV," *Exp. Fluids*, **39**, pp. 743–753.
- [19] Corsini, A., Perugini, B., Rispoli, F., Kinghorn, I., and Sheard, A. G., 2006, "Investigation on Improved Blade Tip Concept," ASME Paper No. GT2006-90592.
- [20] Corsini, A., Rispoli, F., and Sheard, A. G., 2006, "Development of Improved Blade Tip End-Plate Concepts for Low-Noise Operation in Industrial Fans," Proceedings of the Conference on Modeling Fluid Flows CMMF06.
- [21] Corsini, A., Perugini, B., Rispoli, F., Kinghorn, I., and Sheard, A. G., 2007, "Experimental and Numerical Investigations on Passive Devices for Tip-Clearance Induced Noise Reduction in Axial Flow Fans," Proceedings of the Seventh European Conference on Turbomachinery.
- [22] Corsini, A., Perugini, B., Rispoli, F., Sheard, A. G., and Kinghorn, I., 2007, "Aerodynamic Workings of Blade Tip End-Plates Designed for Low-Noise Operation in Axial Flow Fans," ASME Paper No. GT2007-27465.
- [23] Ott, R. L., and Longnecker, M. T., 2000, *An Introduction to Statistical Methods and Data Analysis*, Duxbury, Los Altos, CA.